Ice nucleating activity and residual particle morphology of bulk seawater and sea surface microlayer

Priyatanu Roy[1], Liora E. Mael[2], Thomas C. J. Hill[3], Lincoln Mehndiratta[2], Gordon Peiker[2], Margaret L. House[4], Paul J. Demott[3], Vicki H. Grassian[2], Cari S. Dutcher[1,4,]*

[1]Department of Mechanical Engineering, University of Minnesota Twin Cities, Minneapolis, Minnesota, 55455, United States

[2]Department of Chemistry, University of California, San Diego, La Jolla, California, 92037, United States

[3]Department of Atmospheric Science, Colorado State University, Fort Collins, Colorado, 80523, United States

[4]Department of Chemical Engineering & Materials Science, University of Minnesota Twin Cities, Minneapolis, Minnesota, 55455, United States

KEYWORDS ice nucleating particles, microfluidics, Raman spectroscopy, bulk seawater, sea surface microlayer, sea spray aerosols, efflorescence, morphology

ABSTRACT

Ice nucleating particles (INP) in sea spray aerosols (SSA) are critical in estimating cloud radiative forcing and precipitation with implications in climate change. Laboratory experiments simulating the ocean-atmosphere environment are becoming increasingly popular for studying the nature of INPs in SSAs. Understanding the ice nucleating characteristics of bulk seawater and the sea surface microlayer (SSML) can provide valuable information about the emitted SSA. Samples for this study were collected from a waveflume during a phytoplankton bloom and analyzed with complementary methods. The primary method used is a polydimethylsiloxane (PDMS) based microfluidic static well array, designed and fabricated to trap droplets and measure the ice nucleation (IN) spectra of nanoliter-scale droplets of bulk seawater and SSML. Droplets were subsequently dehydrated *in situ* until efflorescence and dried residual particle morphology was correlated to the droplet IN temperature. Four distinct morphologies were found in the effloresced droplets, among which the aggregate and amorphous morphologies were present in larger amounts in the SSML compared to bulk. These particles also had a different IN spectra, nucleating ice at warmer temperatures than the single and fractal crystal morphologies. The microfluidic studies were complemented by micro-Raman spectroscopy and immersion freezing measurements of larger droplets assessing IN sensitivity to heat and organic carbon removal in an ice spectrometer (IS). This study highlights the compositional diversity of marine samples and paves the way for novel multiplexed microfluidic approaches to study the chemical and biological complexity behind the IN activity of aerosol liquid samples in an integrated platform.

INTRODUCTION

Clouds are key contributors in modulating Earth's climate through their albedo and atmospheric lifetimes [1–3]. Ice nucleating particles (INPs) are a special class of atmospheric particles that facilitate the formation of ice crystals in cloud drops at temperatures warmer than the homogeneous ice nucleation temperature of pure water of -38°C [4]. INPs control the size and concentration of liquid vs. frozen cloud drops [3,5], where clouds comprised of more ice crystals have larger particle sizes and have lower albedo than those composed of mainly liquid drops [6–8], thus shortening cloud lifetime. Ice nucleation also controls precipitation and the water content of clouds by scavenging water vapor from liquid droplets [3,9]. INPs are emitted from various sources, including mineral dusts from arid regions [10,11], from plants and soils, anthropogenic activity [12,13] and, marine sources [5,14].

Oceans cover 71% of the Earth's surface and hence sea spray aerosol (SSA) is potentially a major source of INPs, as well as cloud condensation nuclei (CCN), to the atmosphere [15]. SSA is created by wave breaking, bubble bursting, or through gas phase emissions and secondary organic aerosol formation in the atmosphere [16]. Characterization of marine INP sources is an active area of research for both laboratory and field studies [5,17], and INPs have been measured in bulk seawater as well as the sea surface microlayer (SSML) [18–28]. These studies found that the SSML is more enriched with INPs compared to the bulk overall [19–21] and that the IN activity of SSA can be explained by the INP type and concentration in the underlying bulk seawater and SSML [29]. The exact INP concentration, and the variation of this concentration between the bulk and SSML, depends on multiple factors such as the chemistry of the seawater [29], composition of the SSML [30] and the abundance, size and characteristics of the biogenic INP sources [19,30,31].

In general, surface properties as well as the physical and chemical phase state of an aerosol play an important role in aerosol processes such as ice nucleation (IN), CCN, light scattering and adsorption, and gas-particle partitioning[32]. In IN, the particle size [33,34] and morphology [35,36] have been correlated with IN activity. Specifically, heterogeneous IN at lower temperatures has been shown to be influenced by morphology [37–40] and organic surface coatings [41] of effloresced salt particles. However, these studies have been performed on model or simplified salt solutions. There are very few studies that attempt to correlate the IN property of marine samples with the morphology of the SSA upon collection onto a substrate after drying. In studies measuring IN properties of SSA collected from a waveflume or from smaller tanks, McCluskey et al. [31] and Lee et al. [42] examined the morphology of wet and dried SSA particles on substrates with a scanning electron microscope and atomic force microscope respectively. The INP morphology was correlated to biomarkers such as chlorophyll concentration, and heterotrophic bacteria counts.

The range of instrumentation to study INPs includes both "online" instruments such as continuous flow diffusion chambers [43,44] and continuous flow tubes [45], and "offline" measurements such as differential scanning calorimeters [46], static cold plate based freezing assays [47–49], optical traps [50], and electrodynamic balances [51]. The last two can also be used to observe the phase states (solid, liquid, semi-solid) and morphologies of aerosol particles. Other instruments used to study phase state include optical microscopy with droplets on a substrate [52], tandem differential mobility analyzers [53,54], or particle bounce using impactors [55].

Recently, advances in microfluidic measurements using devices made from a combination of glass and poly-dimethylsiloxane (PDMS) have made it possible to perform IN experiments on a large number of particles using either static [56–58] or flow-based [59–61] approaches. PDMS, being permeable to water, has also led to the construction of trap-based devices where droplet

dehydration and phase transitions can be observed over a long duration in a quasi-equilibrium manner to map out phase states of aerosols at different relative humidities (RH) [62–64]. A recent review by Roy et al. [65] lists different microfluidic devices for droplet-based studies.

For the current work, IN spectra and chemical properties of seawater and SSML are studied with three complementary sets of instrumentation to connect IN spectra with dry-particle morphology as well as biological and organic contributions. Samples were collected during a large multi-institute experiment called SeaSCAPE (Sea Spray Chemistry And Particle Evolution) at the Scripps Institute of Oceanography, La Jolla, CA [66]. A sealed 30m long channel ("waveflume") was filled with coastal Pacific Ocean seawater collected to a depth of 2m. A piston was used to create waves that broke on simulated beach within the waveflume to generate nascent SSA. Both online and offline measurements of SSA and the bulk water were performed using an array of physical, chemical and biological characterization equipment during SeaSCAPE (described in Sauer et al. [66]).

Bulk seawater and SSML samples were collected during various stages of a phytoplankton bloom in the waveflume. A custom microfluidic INP counter and phase transition device was designed based on a recent microwell freezing counter developed by Brubaker et al. [57] and specific IN spectra for a given effloresced particle morphology after drying of the droplets were first measured. This provided a way to investigate correlations between the IN temperature of a droplet and the effloresced residual particle morphology, possibly caused by any potential differences in sample constituents. Micro-Raman spectroscopy was performed on the samples to identify chemical signatures of effloresced bulk and SSML samples. Finally, the INP population in the samples was also measured using an ice spectrometer (IS) that tests large (50 μL) aliquots of solutions, as validation for the microfluidic IN spectra results. In addition, 95°C heat treatment

and peroxide digestion was applied to the SSML samples to highlight the contribution of biogenic and organic INPs respectively.

METHODS AND MATERIALS

Bulk seawater and SSML sample collection

Samples were collected at various stages of an algae bloom from the Scripps Institute of Oceanography waveflume at La Jolla, CA in the summer of 2019 during the SeaSCAPE experiment [66]. The waveflume was filled with coastal seawater from the Pacific Ocean near the Scripps Pier at the start of three SeaSCAPE blooms. The bulk seawater samples were collected using a 2m long siphon made of Teflon tubing and stored in Nalgene carboys precleaned with methanol, ethanol, 0.1 M HCl and ultrapure water. SSML samples were collected using a glass plate, and Teflon scraper. The equipment was rinsed in methanol, ethanol and 10% HCl and baked in a 500°C furnace for 5 hours to remove any organic contaminants prior to sampling. The plate was immersed into the water at 5-6 cm s^{-1} and retracted, then after a 20 s pause to allow water drainage, the scraper was used to scrape off the adhered liquid film into a collection vessel. The resulting sampling thickness was about 50 μm [67]. A subset of the collected liquids from different days during one phytoplankton bloom was shipped frozen to different labs in 50 mL sterile centrifuge tubes for downstream analyses. Samples shown here were primarily collected on July 26, 2019, with data from additional days (August 2, 2019 and August 8, 2019) shown in the ESI. The samples were frozen within 1 hour of collection.

Microfluidic device design and fabrication

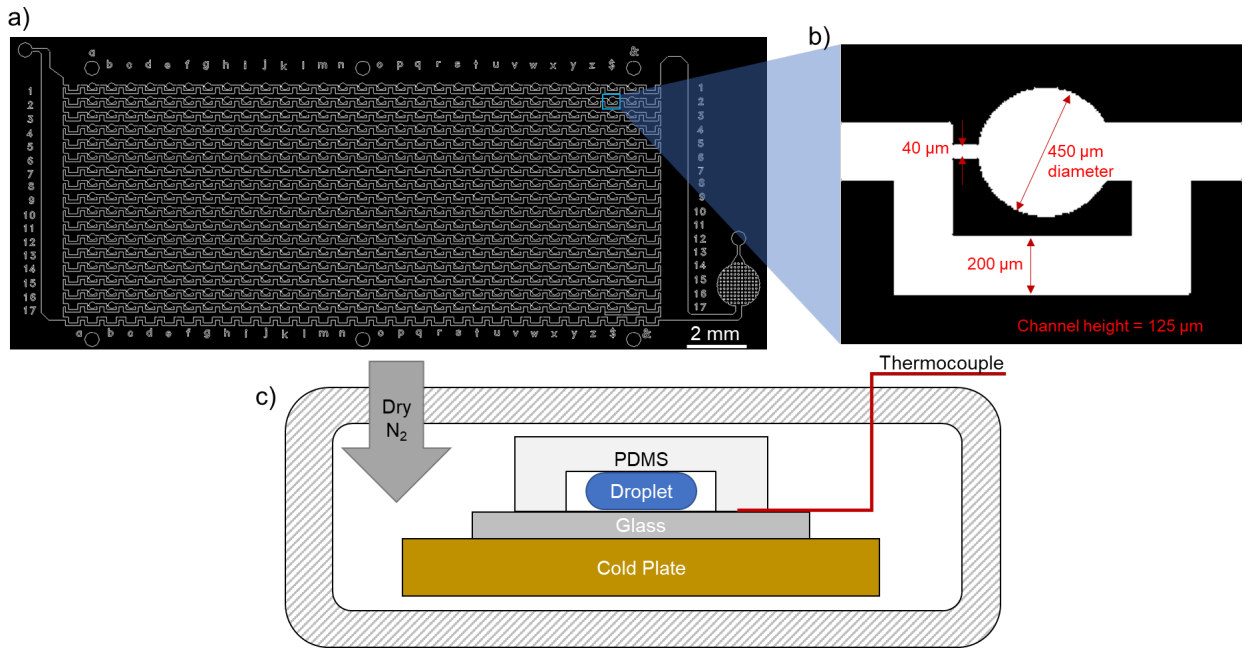

Figure 1: a) Schematic of the static trap-based microfluidic phase and ice nucleation counter device, showing an array of individual wells. b) A close up view of a single well showing the dimensions. c) A schematic of the microfluidic device on the cold plate with dry N_2 gas purging the experimental chamber during a run.

The microfluidic device designed for this study is based on the combination of two static well devices adapted from Sun et al. [68] and Brubaker et al. [57]. The single well shown in Figure 1b was replicated in rows and columns to create a 17x29 grid with 493 separate wells. The wells are connected by an inlet and an outlet to common rails as shown in Figure 1a. There was a filtering region just downstream of the inlet to capture any large (~100 µm) particles and prevent clogging of the device. The design was prepared in AutoCAD (AutoDesk) and printed on a vinyl transparency (CAD/Art Services) to create a photomask. This photomask was used in a standard photolithography process in a cleanroom (MNC) to create a negative mold on a 4" silicon wafer. For this process, a 150µm thick SUEX sheet (DJ Microlaminates) was hot laminated onto the wafer before exposing it to UV light using the photomask and curing the sheet before development. The microfluidic device itself was created by pouring a mixture of PDMS (Sylgard 184, silicone

elastomer, Dow Corning) and the corresponding curing agent in a 10:1 ratio by weight into the silicon wafer mold. PDMS was cured overnight in a 70°C oven before the device was cut out with a razor and holes were punched for the inlet and outlet with a 1.5 mm biopsy punch. Additionally, secondary channels were cut into the device to provide a place for thermocouples during the IN experiment. More details can be found in section 1 of the ESI. For the substrate, a 25x75x1 mm glass slide was coated with PDMS in a spin coater (Laurell) at 3500 rpm for 30 seconds and cured in an oven alongside the mold. The device and the substrate were plasma etched for 60 seconds before pressing them together to form a seal.

Samples were loaded into sterile disposable 1mL syringes (Norm-Ject) fitted with either a 100nm pore-size PTFE syringe filter (Whatman) for pure water background IN experiments or unfiltered in case of SeaSCAPE samples. Following this, silicone oil (Sigma Aldrich) was injected to scavenge out the excess sample from the channels while leaving droplets trapped in the circular wells surrounded by silicone oil. The device also allowed quasi-equilibrium dehydration or rehydration of the droplets after IN measurements due to the permeability of PDMS to water [62–64].

Temperature and RH controlled platform

A temperature-controlled cold plate (LTS 420, Linkam Scientific) was used for the experiments. A glass slide with a mirror layer of 500nm aluminum was placed between the microfluidic device and the cold plate. Thermal paste (Ceramique 2, Arctic Silver) was applied between the mirror slide and the cold plate, and a drop of silicone oil was placed between the device and the mirror slide to ensure good thermal contact while providing the best possible visuals. To provide a wide field of view, the lid supplied with the stage was removed and a custom laser-cut acrylic lid with a rubber gasket on the bottom was used to seal the device from the ambient air. A schematic of the setup is shown in Figure 1c. Dry N_2 gas was introduced into the experiment

chamber through Teflon tubing and a port in the acrylic lid as shown in Figure 1c. For the IN experiments, this prevented condensation of water vapor on the outside of the device. For the phase experiment, during dehydration, this expedited water evaporation from the droplet as the droplet dehydration rate is directly influenced by the RH of the surrounding air.

Microfluidic experimental procedure

During a typical experiment, a pre-calibrated thermocouple (T type, 5SRTC-TT-T-36-36-ROHS, Omega Engineering) was installed inside a precut slit, cut near the center of the device between the top thick PDMS layer and the thin PDMS coated substrate. Device temperature was measured with this thermocouple during each sample measurement. This temperature was verified against melting temperatures of known standard hydrocarbons in the range of -30 to 0°C (see ESI Table S2 for details). Thermocouples placed inside different locations on the device during temperature calibration runs showed a maximum variation of ±0.69°C at -28.85°C and this is reported as the temperature uncertainty of the device. More details on the device temperature measurement process can be found in section 1 of the ESI.

During an experiment, the device was placed on the mirror slide, the top acrylic cover was set in place, and the dry N_2 flow was turned on. Imaging was performed on a reflective microscope (SZX10, Olympus) at different magnification levels and images/videos were recorded with a 1200x1600 px monochromatic camera (acA1600-60gm, Basler)

A flowchart of a typical experiment is shown in Figure 2. IN measurement was done immediately after loading the device with the sample droplets. The microscope was zoomed out to the widest view possible, at which point ~185 droplets were in view simultaneously. Droplets were held at 0°C for 10 minutes for equilibration, and then the temperature of the cold plate was

lowered at 0.5°C min^{-1} using the supplied Link software. Frozen droplets turned darker than liquid droplets.

Following this freezing step, the temperature was brought back to 20°C rapidly and held there for the dehydration experiment. The camera was zoomed in to keep a 3x3 grid of droplets in view. A time lapse video was recorded as the dehydration process happened in a quasi-equilibrium manner over the course of a day. Finally, the camera was zoomed in to single wells and all the residual particles in the device that were observed for the IN experiment were scanned one at a time under the microscope to categorize each into separate morphologies. The bulk and SSML sample from 07-26-2019 were measured using the microfluidic device.

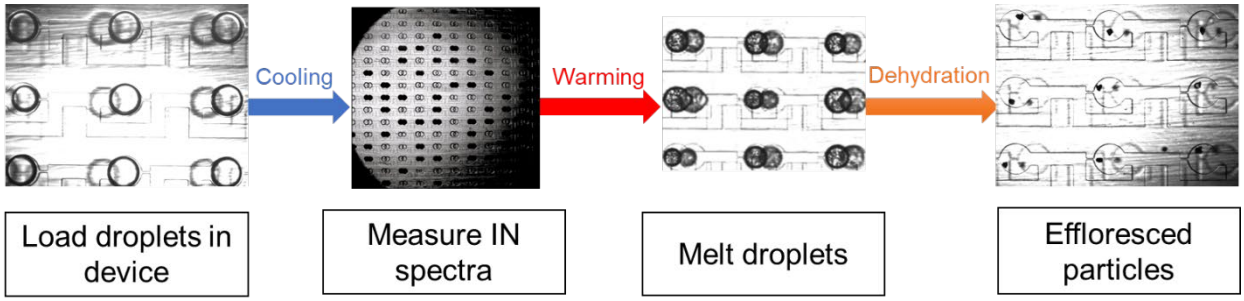

Figure 2: Flowchart of some of the experimental steps performed. The cooling and warming process takes about ~1 hour while the dehydration process often takes >24 hours.

For the IN experiment, frozen fraction of droplets $f(T)$ as a function of temperature T was calculated as

$$f(T) = \frac{N_f(T)}{N_{total}} \qquad 1$$

Where, $N_f(T)$ is the number of wells that are frozen at T and N_{total} is the total number of wells in the view of the camera. The INP concentration in the sample can be calculated using the statistical correlation put forth by Vali[69]:

$$INP(\#/mL^{-1}) = \frac{-\ln(1 - f(T))}{V_{droplet}(mL)} \quad (2)$$

The $V_{droplet}$ refers to the volume of the droplet at the time of observation and was calculated with the following pancake shape assumption [64]:

$$V_{droplet} = \frac{\pi h^3}{6} + \frac{\pi h}{4}(D - h)\left(\frac{\pi h}{2} + D - h\right) \quad (3)$$

Where, D is the observed diameter of the droplet and h is the height of the microfluidic channels (150 μm). Droplets that filled the wells completely had a volume of 21nL. Only droplets within 90% of this maximum were considered for the IN spectra. Measured pure water background spectrum was converted into a background heterogeneous INP concentration using Eq. 2 and subtracted from bulk and SSML sample gross INP counts. Based on literature [21,23,26] on ice nucleation studies with seawater, a standard nominal +2°C correction was applied to undiluted bulk seawater and SSML samples to account for the freezing point depression as the salinity of the water was not measured for this study. Ninety-five percent confidence intervals were obtained from Eq. 2 in Agresti and Coull (1998) [70].

Environmental cell micro-Raman spectroscopy

Chemical composition was obtained with micro-Raman spectroscopy. Frozen Bulk and SSML samples were melted in a warm water bath at T = 30°C. Following this, approximately 1μL droplets of the samples were pipetted onto a hydrophobic substrate. The substrate consists of a quartz disc (Ted Pella, 16001-01) coated with Rain-X. These hydrophobic discs containing the microdroplets were then placed into an environmental cell (Linkam, LTS 120). The cell is coupled to a micro-Raman spectrometer (Horiba, LabRAM HR Evolution) for spectral analysis as previously described in Mael et al. [71]. Once in the environmental cell, the droplets were dried for

12-48 hours under a flow of N_2 at 0.05 L min^{-1} at 25°C prior to data collection, and then held under the same conditions throughout the experiment. Once dried, Raman spectra of different particles of varying morphologies (identified with the Olympus optical microscope fitted to the confocal Raman system) were collected using 10X objective with 3 exposures of 3 seconds averaged for each scan, from 400 to 4000 cm^{-1}.

Ice spectrometer, heat and peroxide treatment

Validating measurements of the microfluidic IN spectra, as well as studies into the role of the biological and organic contributions to the IN ability were obtained using Colorado State University's Ice Spectrometer (IS). The IS measures immersion freezing INPs in aliquots of water arrayed in four 96-well polymerase chain reaction (PCR) plates. These are fitted into aluminum blocks with machined wells and encased by cold plates through which coolant is circulated. The IS produces immersion freezing spectra reaching to -27°C, with a detection limit of 0.6 INPs mL^{-1} and is supported by optimized experimental protocols [43,47,72,73].

To measure INPs in each sample, and in each serial dilution (several 11-fold dilutions made in 0.1 μm-pore-filtered deionized water), 32 aliquots of 50 μL were dispensed into PCR trays (OPTIMUM® ULTRA, Life Science Products) in a laminar flow hood and placed into the cooling blocks. These and a headspace N_2 purge flow were cooled at 0.33 °C min^{-1} using a recirculating low temperature bath, and the freezing of wells recorded. Freezing fraction results were corrected for INPs in the deionized water used for dilutions, and INP temperature spectra were obtained by converting the number of frozen wells at each temperature to the number of INPs mL^{-1} using Eq. 2.

Tests were performed to estimate heat-labile (e.g., proteins) and total organic INPs. For the former, 2 mL of SSML were heated to 95°C for 20 min and the sample re-analyzed to measure the

reduction in INPs. To quantify organic INPs, 1 mL of 30% H_2O_2 (Sigma) was mixed with 2 mL of sample and digested at 95°C for 20 min under UV-B. This and decomposition of residual H_2O_2 are detailed in Suski et al. [74]. The sample was then re-analyzed in the IS to measure the reduction after the removal of organic INPs.

RESULTS

Microfluidic IN spectra

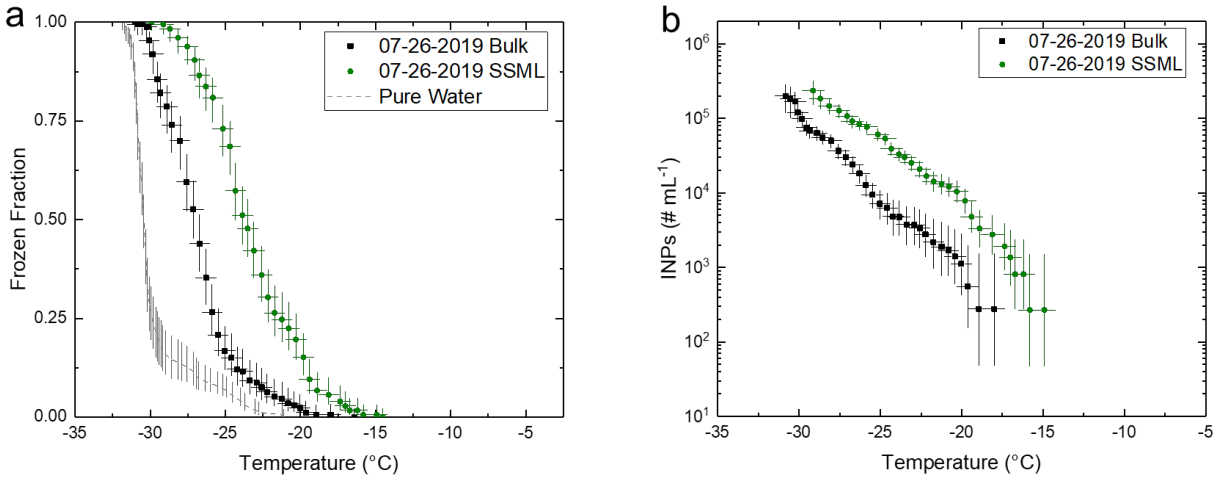

Figure 3: IN spectra measured using the microfluidic device from bulk and SSML of 07-26-2019. (a) Frozen fraction as a function of temperature, calculated from the fraction of wells frozen out of all wells in the view of the camera at any given temperature. The gray line represents the background pure water spectra. The background was collected after loading the device with a syringe of deionized water fitted with a 0.1um PTFE syringe filter. (b) The bulk and SSML samples expressed as INPs ml^{-1}. Vertical error bars indicate 95% confidence interval. Horizontal error bars indicate uncertainty of ±0.69°C in temperature measurement from thermocouples. The curves have been corrected for freezing point depression.

IN data of the bulk and SSML collected with the microfluidic device are shown in Figure 3. The horizontal error bars represent uncertainty in temperature measurement from the thermocouples. The pure water ice nucleation background spectra is plotted in Figure 3a and shows a freezing curve spanning around 10°C (between -21 and -31°C) with a steep rise below -30°C. The median freezing temperature for ultrapure water in this device is -30.3°C. This curve has a

similar shape and freezing temperature range to other droplet based IN counters [56,57,75]. The temperature range of the background spectra indicates heterogeneous nucleation, either from contaminants in the water or from contact with particles and/or the surfaces already present inside the device. This heterogeneous background freezing shown in Figure 3a restricts the device to analyze samples that freeze above the temperature -30°C.

A prominent feature of these graphs is that the gap in INP concentrations (Figure 3b) between the bulk and the SSML is about an order of magnitude at temperatures >-26°C. This enrichment in INPs in the SSML may also indicate a compositional difference, and to explore this, the droplets were dried after the IN spectra measurement to investigate any overall trends in the efflorescent particle morphologies. The microfluidic device allows droplet dehydration directly after IN spectra measurement, without having to transport the droplets to a new device. The connection between the freezing temperatures of the individual droplets and the effloresced particle morphologies was investigated as explained in the following section.

Effloresced particle morphology

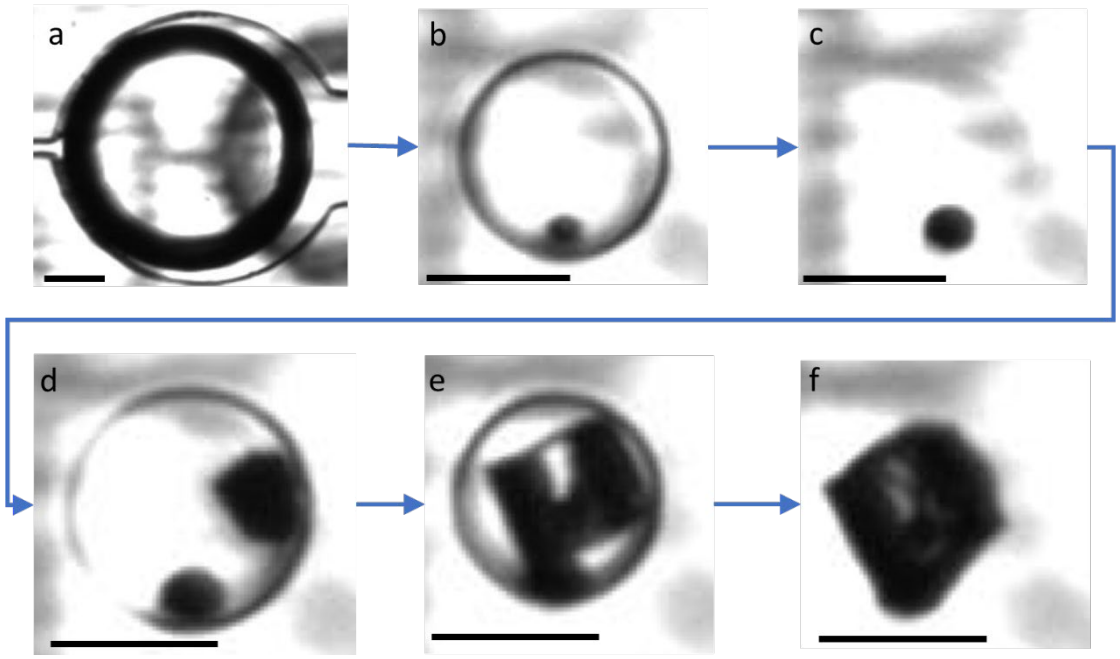

Figure 4: (a-f) Droplet morphologies observed in a bulk seawater droplet from 07-26-2019 dehydrating inside a microfluidic well. The arrow indicates the progression of the experiment. A particle nucleates in panel b and its size remains relatively constant throughout the rest of the dehydration process. The refractive index of the droplet matches the surrounding silicone oil in panel c. A new salt crystal, possibly NaCl, nucleates in panel d and keeps growing into a larger cubic crystal until panel f where a translucent coating forms over the whole dry particle. Scale bars in the images are 100µm.

The droplet dehydration process is shown in Figure 4. Note that the reflection of the droplet from the mirror surface below gives the appearance of an apparent "doubled" droplet in Figure 4. This is an image artifact, not a separate droplet. The fresh, or just-loaded, droplet in Figure 4a is relatively large and slowly dehydrates until it reaches the state shown in Figure 4b. At this point, a small darker particle emerges from the liquid, and the whole droplet keeps shrinking as it evaporates until it reaches the state in Figure 4c. Here, the droplet disappears from view due to the refractive index of the liquid in the droplet matching the refractive index of the surrounding oil. Following this, the droplet continues to shrink and reappears into view as a second particle emerges from a different spot in Figure 4d. The second particle grows and forms a transparent cubic shape as seen in Figure 4e. This is an NaCl crystal and has a cubic crystalline structure. Near the very end of the dehydration process, a translucent coating appears to form and cover the whole dry

particle as shown in Figure 4f. The main part of the dehydration process from Figure 4a to b takes about 24 hours, and the remaining part from b to f takes around an hour.

Figure 5(a-d) shows the types of residual particle morphologies observed after an efflorescence experiment. The single crystal morphology has a single large cubic crystal of NaCl surrounded by a more amorphous coating or other much smaller crystals, as evident from the transitions shown in Figure 4. The fractal crystal morphology has multiple medium sized crystals growing in different orientations in a jagged geometric repeating pattern, possibly indicating nucleation from multiple sources through smaller particles present in the droplets. The aggregate particle morphology has almost a circular shape with many small crystals, forming the outer surface of the particle. The amorphous morphology is assigned to particles that have no discernible crystalline

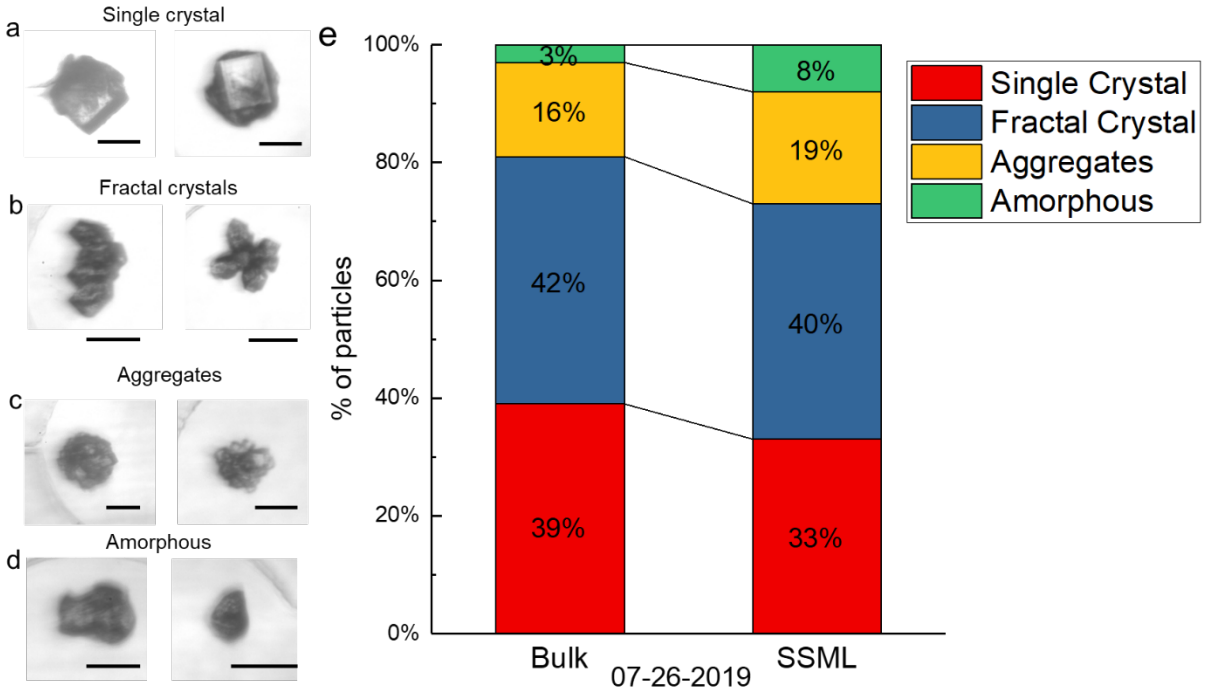

Figure 5: (a-d) Typical effloresced droplet morphologies observed in microfluidic wells after complete droplet dehydration. Scale bars in the images represent 50 µm. (e) Droplet morphologies represented as a fraction of total droplet count observed in each sample. The samples contained 405 and 390 total particles respectively.

shape on the outside, which possibly indicates a larger amount of detritus or organics in the initial droplet. These form a thicker or more irregular coating on the outside of salt crystals inside the

particle, thus concealing them. The distribution of different particle types formed after efflorescence is shown in Figure 5e. The total particle counts for droplet morphology were 405 and 390 in the bulk and SSML samples respectively. The IN spectra for the bulk and SSML samples considers smaller subsets of total 173 and 178 droplets respectively. The differences in the number of droplets analyzed in the morphology and IN spectra are due to the IN measurement requiring particles to be in the camera field of view simultaneously during the experiment, while the morphology of the particle could be measured post-experiment by moving the XY stage of the microscope one at a time under the camera. Hence, for the morphology measurement, all the particles loaded into the device could be examined. The bulk sample has a slightly larger fraction of single and fractal crystal particle types when compared to the aggregate and amorphous particles. Similar morphology results were obtained for samples from other days (08-02-2019 and 08-06-2019), shown in Figure S3 in the ESI. In all cases, SSML contains more aggregate and amorphous samples, while the bulk contains more fractal and single crystal structures.

Statistical significance between the different particle types were tested using Z scores for two population proportions. The significance level between similar particle types between samples are shown in the P values in Table S3 in the ESI, where there is a trend towards increased aggregate and amorphous particles in the SSML sample compared to the bulk. For 07-26-2019, when the aggregate and amorphous types are combined into a single 'non-crystalline' group, there is a statistically significant difference between the bulk and SSML ($P = 0.008$). Likewise, a combined single and fractal crystal group shows statistically significant reduction of crystalline morphologies in the SSML sample compared to the bulk. Similar trends were observed for the other dates, though the calculated P values were greater than 0.05. Further discussion can be found in the ESI.

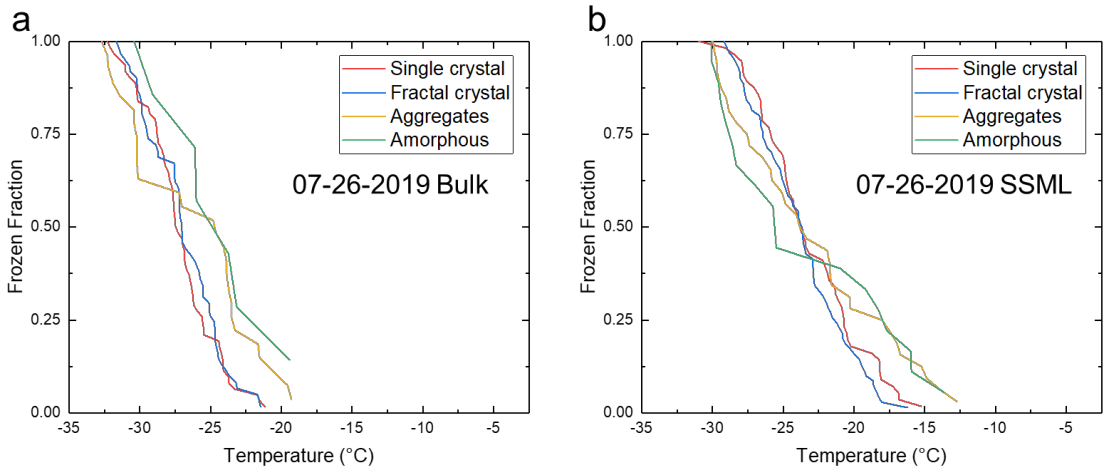

Figure 6: Frozen fraction curves of each droplet morphology for a given sample. a) 07-26-2019 bulk, b) 07-26-2019 SSML. The samples contained 173 and 178 droplets respectively.

The freezing temperatures of the droplets in a subset of the microfluidic wells were connected to the effloresced particle morphology and the resulting frozen fraction curves for each particle type are plotted in Figure 6. From the subpanels it is apparent that there is no significant difference in the IN temperatures of the single crystal vs. the fractal crystal types in both bulk and SSML. However, in both samples, the aggregates and the amorphous category curves start freezing at a warmer temperature than the single or fractal crystal droplets. They also generally have different freezing curves with more gradual slopes, leading to freezing over a broader temperature range compared to the single and fractal crystal particles. This perhaps indicates that the liquid droplets in these wells contained a more heterogeneous mix of contents contributing a diverse freezing range of INPs, requiring further chemical identification as described in the next section.

Chemical signatures of particles

Between 30 and 40 particles were analyzed in the micro-Raman spectroscope for each sample. Spectral and optical data for dried droplets from SSML and bulk seawater from the three days are shown in Figure 7. All the spectral features identified here were found in different particles in both

bulk and SSML samples, and representative of the spectra and morphology found in all three days. While this work clearly informs the chemical signature of the samples in general, unique connections between morphology and Raman spectra cannot yet be made. Many particles (spectra 1-7) contain sulfate, identified by the sulfate symmetric stretch ranging from 950 to 1100 cm^{-1} (highlighted in orange). The exact frequency of this vibrational mode depends on several factors including the coordinating cation (Na^{+}, Ca^{2+} and Mg^{2+}) and hydration state [76,77]. In addition to sulfate, particles corresponding to spectra 3 and 5 showed the presence of carotenoids as indicated by the two peaks at 1522 and 1154 cm^{-1} (highlighted in purple) [78]. Several particles exhibit vibrational peaks indicative of organic compounds (shown in spectra labeled 4, 5, 7) in addition to sulfate (highlighted in green). The amount of organics present in the spectrum labeled "5" is much higher than in other spectra. This has been identified as sialic acid as discussed in previous studies [77,79]. Many particles were identified as sodium chloride (spectrum 8) and were found in both bulk and SSML as well. These particles were identified because they have no Raman bands in the region investigated, and in many cases, clear salt crystal shapes were observed in the optical image. All particle spectra identified (1-8) most likely contain various amounts of NaCl, but due to the lack of spectral signature this cannot be quantified. Section 5 in the ESI contains a table summarizing the Raman spectra assignments.

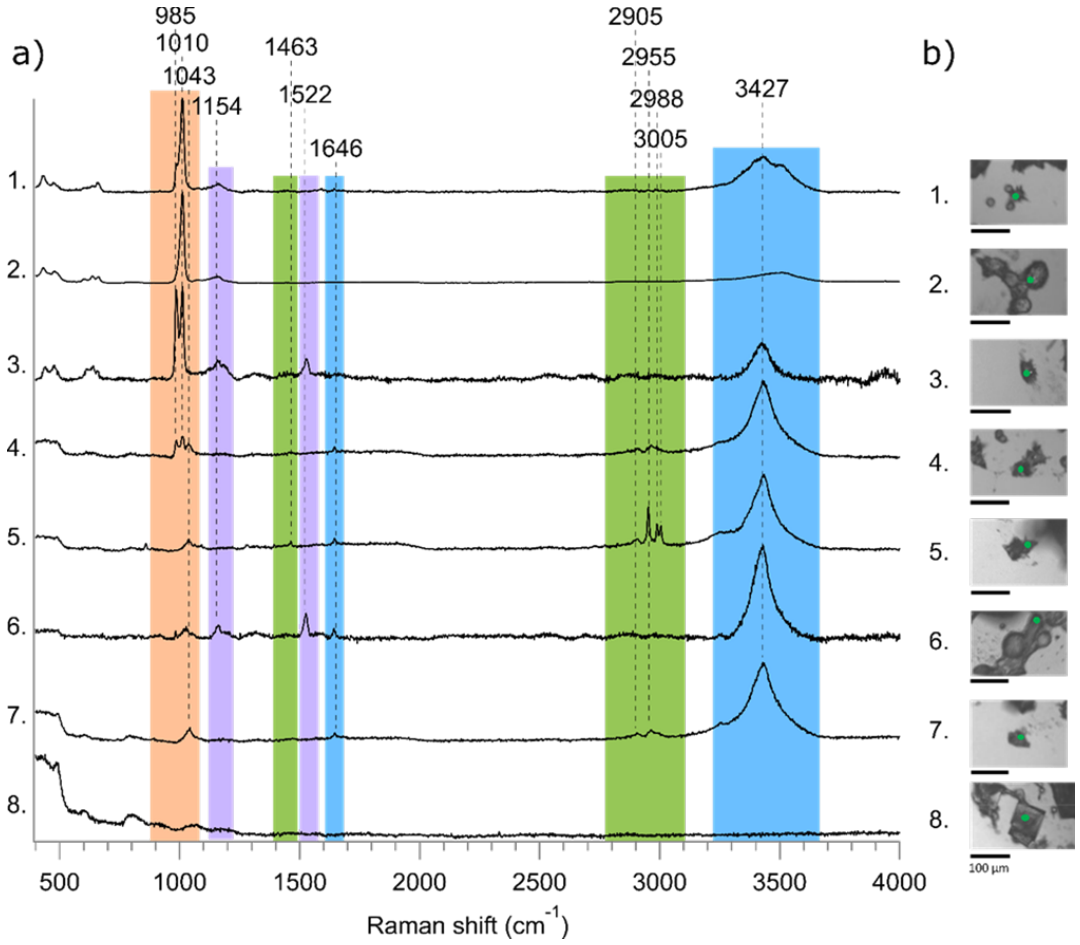

Figure 7: Results from representative (a) spectra and corresponding (b) optical images from dried SSML and bulk single particles. Different color bands highlight the significant spectral regions and peaks that correspond with literature values of sulfate (orange), carotenoids (purple), other organic compounds (green), possibly sialic acid (5), and water (blue). Green dots on the optical images indicate the location spectra were collected.

Heat treatment and H_2O_2 oxidation results

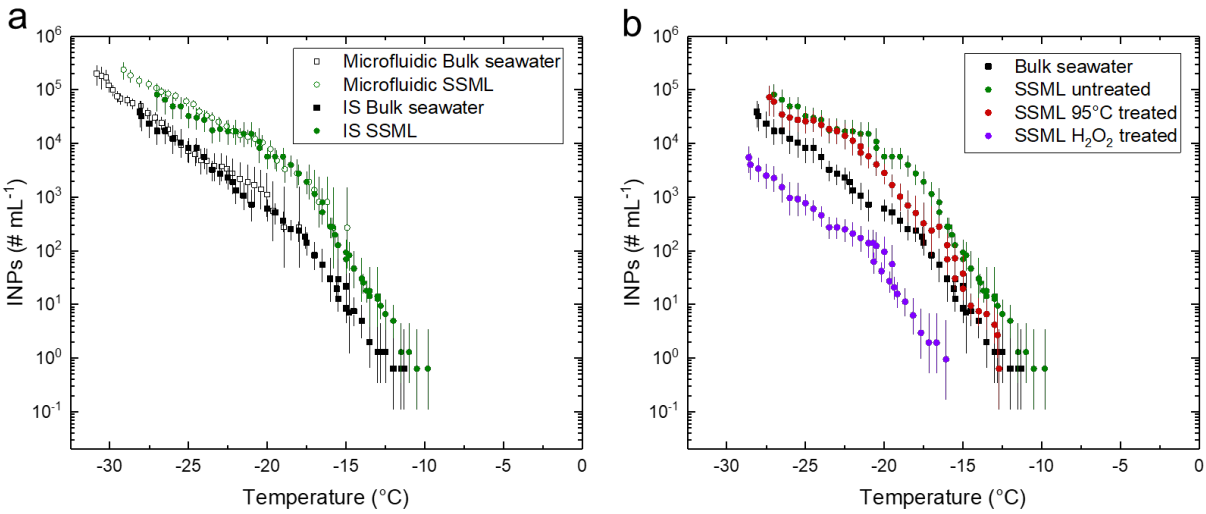

Figure 8: (a) Intercomparison of INP counts in bulk and SSML between microfluidic device and IS The microfluidic data is reproduced from Figure 3b. (b) IS measured INP counts in SSML and bulk seawater for nominal, 95°C heat-treated and H_2O_2 digested sample. The data was collected with the automated ice spectrometer using a 96 well plate. The curves have been corrected for freezing point depression. The error bars represent 95% confidence intervals.

Finally, Figure 8a,b shows the INP counts in bulk and SSML samples measured with the IS using 50 µL aliquots. The microfluidic device IN spectra has been reproduced in Figure 8a to compare with the IS measurements of untreated bulk and SSML samples. In the regions of overlap between the two methods (from around -15 to -28°C) there was very close agreement in both INP concentrations and spectral curvature for both bulk and SSML samples. As seen with both measurements, there is a significant enrichment of INPs in the SSML. Figure 8b shows the INP counts after treatment of the SSML samples by heating at 95°C and after peroxide digestion. Specifically, the red circles show that a significant portion of INPs active above -22°C in the SSML were moderately heat sensitive and deactivated after heating at 95°C due to their biological nature. The purple circles show that after H_2O_2 oxidation, which targets organic INPs, at least 98% of INPs were deactivated compared to the untreated SSML. In this case, the INP count was lower

than even the bulk seawater, indicating that a major part of the INP population in both bulk and SSML was likely organic.

DISCUSSION

Previous studies on the ice nucleating properties of SSML and bulk seawater on field or lab-generated samples show that there is usually large variability in the ice nucleation temperature even in a single study [19,21,28–30,80]. The variations arise from different conditions at the sampling locations such as the water chemistry, local biological activity, SSML composition, and the sampling method employed. In particular, results in SSA and seawater (both bulk and SSML) collected from waveflumes[30,31] have shown significant variability in the IN properties before, during and after a phytoplankton bloom. The bulk and SSML INP counts reported with both the IS and the microfluidic device reported here are within the range reported in previous studies on bulk seawater [19,21,23,24,28,29,31] as well as SSML [20,28–31,80].

The microfluidic ice nucleation results show clear differences in the INP concentration between the bulk and SSML samples, indicating significant enrichment compared to the bulk. Similar results have been reported previously [80]. Marine biological entities such as heterotrophic bacteria[81], phytoplankton [27,82], surface active organics[20] and gels are enriched in the SSML.

The morphologies of effloresced particles observed in the microfluidic wells are broadly equivalent to the particle types observed in previous studies on SSA impacted onto substrates and imaged with atomic force microscopy [42] or scanning electron microscopy [31], i.e. crystalline, aggregates and amorphous entities. Due to the high salt content of sea water, the microfluidic results show aggregate and amorphous morphology particle counts that are much smaller in number compared to the single and fractal crystal morphologies, the latter two types making up

81% and 73% of the particles in the bulk and SSML samples, respectively. IN temperatures of the aggregate and amorphous morphologies are spread over a wider range of temperatures than the single and fractal crystals. Similarly, both the amorphous and aggregates morphologies have several degree warmer onset temperatures of freezing than the other types. However, while the freezing of the non-crystalline particles does initiate at a warmer temperature, the IN spectra does not lie completely to the warmer side of the crystalline particles. We feel further investigations with model INPs are necessary to systematically investigate the correlation between residual droplet morphology and IN temperature in microfluidic wells.

The differences in morphology signify an excess amount of organic material present in the droplets that effloresced into aggregate and amorphous particles, perhaps related to an inhomogeneity present in the specific well or departure from the overall average composition of the sample as a whole. This may indicate the presence of larger gels. The single and fractal crystal particle freezing curves in both bulk and SSML samples have similar slopes and overall nucleate at colder temperatures and with a smaller spread, indicating more homogeneous and perhaps inorganic salt contents in the droplets. Further investigation of the chemical composition was determined with environmental micro-Raman spectroscopy on effloresced residual particles formed from microliter droplets. The Raman spectra show NaCl, sulfate, carotenoids, and other organic compounds in particles from both the bulk and the SSML collected from the same day as those used in the microfluidic experiments. These samples also included residual particles containing some unique signatures of sulfate hydrate salts with organics with peaks in the region 2905-3005 cm^{-1}. Some of these particles included sialic acid which was not present in the bulk. Sialic acid has been identified as an algae synthesized product [83], and hence its presence in the samples is not surprising for these seawater-based samples.

Finally, heat and peroxide treatments further differentiated the heat-labile (i.e., biological) and total organic components of the INP populations. There was a moderate reduction of INPs after heat treatment but a further very large decrease after peroxide digestion. This indicated that the INP population in the SSML consisted a mix of heat-labile biological entities and heat-stable organic INPs (only 0.5-2% of INPs were inorganic). Interestingly, the peroxide treatment also reduced the INP count below that of the bulk seawater, suggesting that the bulk also contained a significant amount of organic INPs. This generally agrees with previously observed trends of larger amounts of biological and organic INPs present in SSML samples compared to bulk samples [19,20,31], which also deactivated with heat [19–21,31]. The sample analyzed here (07-26-2019) is from relatively fresh seawater, sampled three days after the filling of the waveflume. A significant heat sensitive INP population in the was found in the SSML at >-20°C, which is also the temperature range where the amorphous and aggregate residual particles start freezing earlier than the single and fractal crystal particles in the microfluidic device. This result is indicative of higher amounts of the warmer INPs in the former morphologies. IS results and effects of heat and peroxide treatments from two other sample days (08-02-2019 and 08-06-2019) are presented and detailed in section 3 of the ESI.

A future study is planned to perform these treatments on droplets already loaded into the microfluidic chip to observe potential links between IN temperature and morphology between treated and untreated samples. Confocal Raman spectroscopy could also be integrated inside the platform [64] to establish more direct connections between morphology and chemical composition of particles.

CONCLUSIONS

In this work, the IN characteristics were connected to particle morphology and composition of bulk seawater and SSML from the SeaSCAPE study, using a microfluidic method complemented by ice spectrometry and micro-Raman spectroscopy measurements.

For the microfluidic method, a grid of microfluidic wells was used in a PDMS-based device to create ~20 nL droplets and study their ice nucleation temperature. The grid allowed the correlation of the temperature at which ice nucleated with the morphology of the particle. Upon drying, bulk and SSML samples from the same day showed broadly four different morphologies: single crystal, fractal crystal, aggregates and amorphous. The single crystal and fractal crystal types were present in a larger fraction of the particles in the bulk sample compared to the SSML sample. When the ice spectra of the samples were analyzed according to particle morphology, it was found that, droplets which effloresced into aggregate and amorphous particles started freezing at warmer temperatures compared to the other two types. Indicating perhaps the presence of a characteristic unique organic material (e.g. gels) compared to the largest fraction of drops which effloresced into the single and fractal crystal morphologies.

Micro-Raman spectroscopy of dried microliter droplets of SSML and bulk seawater showed the presence of sulfates, organic compounds identified in some cases as carotenoids and sialic acid, and sodium chloride. Pure sodium chloride crystals were identified as well. These different chemical signatures were present in the bulk and SSML. Ice nucleation was also measured with a ice spectrometer. The nominal INP counts had excellent correspondence with the microfluidic IN results. The SSML sample was additionally measured after heat treatment at 95°C and H_2O_2 digestion to differentiate heat-labile biological INPs and organic matter respectively. INPs in the SSML were mostly heat sensitive. ~~but almost entirely organic.~~ The aggregate and amorphous

morphology ice spectra from the microfluidic measurements also showed some enrichment of warmer, and possibly heat sensitive, INPs in the SSML.

This study, for the first time, utilizes a microfluidic device to investigate both phase transitions and ice nucleation characteristics of aqueous droplets, and provides a platform to correlate effloresced residual particle morphology to droplet ice nucleation temperature. The microfluidic device results were complemented with ice spectrometer results, with heat treatment and oxidation of the bulk and SSML samples, to isolate contributions of heat-labile and insensitive organic INPs to the samples and micro-Raman spectroscopy to identify the chemical makeup of the effloresced particles. In future studies, the microfluidic device can be modified with only minor changes to integrate both heating and Raman spectroscopy in a combined single setup. This will increase ease of use and reduce variability among samples and measurement methods. The microfluidic platform shown here has the potential to perform these studies with an order of magnitude reduction in sample volume and shorter processing time compared to microliter sized droplet-based methods. Ultimately, it can contribute significantly to the field of atmospheric chemistry by providing a simple and versatile alternative to traditional aerosol instrumentation.

ASSOCIATED CONTENT

Electronic Supporting Information (ESI)

This electronic supplementary material contains: 1) Description of the temperature measurement process of the microfluidic device. 2) Particle morphology data from additional days during the phytoplankton bloom. 3) IS measured INP data and statistical analysis from additional

days during the phytoplankton bloom. 4) Table of Raman spectra peak wavenumbers and corresponding chemical bond assignments.

AUTHOR INFORMATION

Corresponding Author

*E-mail: cdutcher@umn.edu

Author Contributions

The manuscript was written through contributions of all authors. All authors have given approval to the final version of the manuscript.

ACKNOWLEDGEMENT

This work was supported by NSF through the NSF Center for Aerosol Impacts on Chemistry of the Environment (CAICE), an NSF Funded Center for Chemical Innovation (CHE-1801971), NSF Graduate Research Fellowship Program (DGE-1650112) for support of L.M. Portions of this work were conducted in the Minnesota Nano Center, which is supported by the National Science Foundation through the National Nano Coordinated Infrastructure Network, Award Number NNCI -1542202. The authors would like to the thank the whole SeaSCAPE team for their contributions to the sample collection and coordination efforts throughout this work. The samples measured by T.H. were provided by Josephine Rudd. to Any opinions, findings, and conclusions or recommendations expressed in this material are those of the authors and do not necessarily reflect the views of the National Science Foundation.

ABBREVIATIONS

CCN, cloud condensation nuclei; IN, ice nucleation; INP, ice nucleating particle; IS, ice spectrometer; PCR, polymerase chain reaction; PDMS, polydimethylsiloxane; RH, relative humidity; SeaSCAPE, Sea Spray Chemistry And Particle Evolution; SSA, sea spray aerosol; SSML, sea surface microlayer

REFERENCES

(1) Stevens, B.; Boucher, O. Climate Science: The Aerosol Effect. *Nature* **2012**, *490* (7418), 40–41. https://doi.org/10.1038/490040a.

(2) Boucher, O.; Randall, D. A.; Artaxo Netto, P. E.; Bretherton, C.; Feingold, G.; Forster, P.; Kerminen, V.-M.; Kondo, Y.; Liao, H.; Lohmann, U.; Rasch, P.; Satheesh, S. K.; Sherwood, S.; Stevens, B.; Zhang, X.; Fuzzi, S.; Penner, J. E.; Ramaswamy, V.; Stubenrauch, C. Clouds and Aerosols. In *Climate Change 2013 – The Physical Science Basis: Working Group I Contribution to the Fifth Assessment Report of the Intergovernmental Panel on Climate Change*; Cambridge University Press: Cambridge, 2013; pp 571–658. https://doi.org/10.1017/CBO9781107415324.016.

(3) Pruppacher, H. R.; Klett, J. D. *Microphysics of Clouds and Precipitation*; Springer Netherlands, 1997. https://doi.org/10.1007/978-94-009-9905-3.

(4) Pruppacher, H. R. A New Look at Homogeneous Ice Nucleation in Supercooled Water Drops. *J. Atmos. Sci.* **2002**, *52* (11), 1924–1933. https://doi.org/10.1175/1520-0469(1995)052<1924:anlahi>2.0.co;2.

(5) Kanji, Z. A.; Ladino, L. A.; Wex, H.; Boose, Y.; Burkert-Kohn, M.; Cziczo, D. J.; Krämer,

M. Overview of Ice Nucleating Particles. *Meteorol. Monogr.* **2017**, *58*, 1.1-1.33. https://doi.org/10.1175/AMSMONOGRAPHS-D-16-0006.1.

(6) Twomey, S. The Influence of Pollution on the Shortwave Albedo of Clouds. *J. Atmos. Sci.* **1977**, *34* (7), 1149–1152. https://doi.org/10.1175/1520-0469(1977)034<1149:TIOPOT>2.0.CO;2.

(7) DeMott, P. J.; Prenni, A. J.; Liu, X.; Kreidenweis, S. M.; Petters, M. D.; Twohy, C. H.; Richardson, M. S.; Eidhammer, T.; Rogers, D. C. Predicting Global Atmospheric Ice Nuclei Distributions and Their Impacts on Climate. *Proc. Natl. Acad. Sci. U. S. A.* **2010**, *107* (25), 11217–11222. https://doi.org/10.1073/pnas.0910818107.

(8) Korolev, A.; McFarquhar, G.; Field, P. R.; Franklin, C.; Lawson, P.; Wang, Z.; Williams, E.; Abel, S. J.; Axisa, D.; Borrmann, S.; Crosier, J.; Fugal, J.; Krämer, M.; Lohmann, U.; Schlenczek, O.; Schnaiter, M.; Wendisch, M. Mixed-Phase Clouds: Progress and Challenges. *Meteorol. Monogr.* **2017**, *58* (1), 5.1-5.50. https://doi.org/10.1175/amsmonographs-d-17-0001.1.

(9) Seinfeld, J. H.; Pandis, S. N. *Atmospheric Chemistry and Physics: From Air Pollution to Climate Change*; 2006. https://doi.org/10.1063/1.882420.

(10) Hoose, C.; Möhler, O. Heterogeneous Ice Nucleation on Atmospheric Aerosols: A Review of Results from Laboratory Experiments. *Atmos. Chem. Phys. Discuss.* **2012**, *12* (5), 12531–12621. https://doi.org/10.5194/acpd-12-12531-2012.

(11) Murray, B. J.; O'sullivan, D.; Atkinson, J. D.; Webb, M. E. Ice Nucleation by Particles Immersed in Supercooled Cloud Droplets. *Chem. Soc. Rev.* **2012**, *41* (19), 6519–6554. https://doi.org/10.1039/c2cs35200a.

(12) Hill, T. C. J.; Demott, P. J.; Tobo, Y.; Fröhlich-Nowoisky, J.; Moffett, B. F.; Franc, G. D.; Kreidenweis, S. M. Sources of Organic Ice Nucleating Particles in Soils. *Atmos. Chem. Phys.* **2016**, *16* (11), 7195–7211. https://doi.org/10.5194/acp-16-7195-2016.

(13) Garcia, E.; Hill, T. C. J.; Prenni, A. J.; DeMott, P. J.; Franc, G. D.; Kreidenweis, S. M. Biogenic Ice Nuclei in Boundary Layer Air over Two U.S. High Plains Agricultural Regions. *J. Geophys. Res. Atmos.* **2012**, *117* (17), 1–12. https://doi.org/10.1029/2012JD018343.

(14) DeMott, P. J.; Hill, T. C. J.; McCluskey, C. S.; Prather, K. A.; Collins, D. B.; Sullivan, R. C.; Ruppel, M. J.; Mason, R. H.; Irish, V. E.; Lee, T.; Hwang, C. Y.; Rhee, T. S.; Snider, J. R.; McMeeking, G. R.; Dhaniyala, S.; Lewis, E. R.; Wentzell, J. J. B.; Abbatt, J.; Lee, C.; Sultana, C. M.; Ault, A. P.; Axson, J. L.; Diaz Martinez, M.; Venero, I.; Santos-Figueroa, G.; Stokes, M. D.; Deane, G. B.; Mayol-Bracero, O. L.; Grassian, V. H.; Bertram, T. H.; Bertram, A. K.; Moffett, B. F.; Franc, G. D. Sea Spray Aerosol as a Unique Source of Ice Nucleating Particles. *Proc. Natl. Acad. Sci. U. S. A.* **2016**, *113* (21), 5797–5803. https://doi.org/10.1073/pnas.1514034112.

(15) Lewis, E. R.; Schwartz, S. E. Sea Salt Aerosol Production: Mechanisms, Methods, Measurements and Models—A Critical Review. In *Geophysical Monograph Series*; Geophysical Monograph Series; American Geophysical Union: Washington, D. C., 2004; Vol. 152, pp 1–408. https://doi.org/10.1029/152GM01.

(16) Cochran, R. E.; Ryder, O. S.; Grassian, V. H.; Prather, K. A. Sea Spray Aerosol: The Chemical Link between the Oceans, Atmosphere, and Climate. *Accounts of Chemical Research*. March 21, 2017, pp 599–604. https://doi.org/10.1021/acs.accounts.6b00603.

(17) Brooks, S. D.; Thornton, D. C. O. Marine Aerosols and Clouds. *Ann. Rev. Mar. Sci.* **2018**, *10*, 289–313. https://doi.org/10.1146/annurev-marine-121916-063148.

(18) Fall, R.; Schnell, R. C. Association of an Ice-Nucleating Pseudomonad with Cultures of the Marine Dinoflagellate, Heterocapsa Niei. *J. Mar. Res.* **1985**, *43* (1), 257–265. https://doi.org/10.1357/002224085788437370.

(19) Irish, V. E.; Hanna, S. J.; Xi, Y.; Boyer, M.; Polishchuk, E.; Ahmed, M.; Chen, J.; Abbatt, J. P. D.; Gosselin, M.; Chang, R.; Miller, L. A.; Bertram, A. K. Revisiting Properties and Concentrations of Ice-Nucleating Particles in the Sea Surface Microlayer and Bulk Seawater in the Canadian Arctic during Summer. *Atmos. Chem. Phys.* **2019**, *19* (11), 7775–7787. https://doi.org/10.5194/acp-19-7775-2019.

(20) Wilson, T. W.; Ladino, L. A.; Alpert, P. A.; Breckels, M. N.; Brooks, I. M.; Browse, J.; Burrows, S. M.; Carslaw, K. S.; Huffman, J. A.; Judd, C.; Kilthau, W. P.; Mason, R. H.; McFiggans, G.; Miller, L. A.; Najera, J. J.; Polishchuk, E.; Rae, S.; Schiller, C. L.; Si, M.; Temprado, J. V.; Whale, T. F.; Wong, J. P. S.; Wurl, O.; Yakobi-Hancock, J. D.; Abbatt, J. P. D.; Aller, J. Y.; Bertram, A. K.; Knopf, D. A.; Murray, B. J. A Marine Biogenic Source of Atmospheric Ice-Nucleating Particles. *Nature* **2015**, *525* (7568), 234–238. https://doi.org/10.1038/nature14986.

(21) Irish, V. E.; Elizondo, P.; Chen, J.; Choul, C.; Charette, J.; Lizotte, M.; Ladino, L. A.; Wilson, T. W.; Gosselin, M.; Murray, B. J.; Polishchuk, E.; Abbatt, J. P. D.; Miller, L. A.; Bertram, A. K. Ice-Nucleating Particles in Canadian Arctic Sea-Surface Microlayer and Bulk Seawater. *Atmos. Chem. Phys.* **2017**, *17* (17), 10583–10595. https://doi.org/10.5194/acp-17-10583-2017.

(22) Rosinski, J.; Haagenson, P. L.; Nagamoto, C. T.; Quintana, B.; Parungo, F.; Hoyt, S. D. Ice-Forming Nuclei in Air Masses over the Gulf of Mexico. *J. Aerosol Sci.* **1988**, *19* (5), 539–551. https://doi.org/10.1016/0021-8502(88)90206-6.

(23) Schnell, R. C. Ice Nuclei in Seawater, Fog Water and Marine Air off the Coast of Nova Scotia: Summer 1975. *J. Atmos. Sci.* **1977**, *34* (8), 1299–1305. https://doi.org/10.1175/1520-0469(1977)034<1299:inisfw>2.0.co;2.

(24) Schnell, R. C.; Vali, G. Freezing Nuclei in Marine Waters. *Tellus* **1975**, *27* (3), 321–323. https://doi.org/10.3402/tellusa.v27i3.9911.

(25) Parker, L. V; Sullivan, C. W.; Forest, T. W.; Ackley, S. F. Ice Nucleation Activity of Antarctic Marine Microorganisms. *Antarct. J.* **1985**, *20*, 126–127.

(26) Creamean, J. M.; Cross, J. N.; Pickart, R.; McRaven, L.; Lin, P.; Pacini, A.; Hanlon, R.; Schmale, D. G.; Ceniceros, J.; Aydell, T.; Colombi, N.; Bolger, E.; DeMott, P. J. Ice Nucleating Particles Carried From Below a Phytoplankton Bloom to the Arctic Atmosphere. *Geophys. Res. Lett.* **2019**, *46* (14), 8572–8581. https://doi.org/10.1029/2019GL083039.

(27) Wilbourn, E. K.; Thornton, D. C. O.; Ott, C.; Graff, J.; Quinn, P. K.; Bates, T. S.; Betha, R.; Russell, L. M.; Behrenfeld, M. J.; Brooks, S. D. Ice Nucleation by Marine Aerosols Over the North Atlantic Ocean in Late Spring. *J. Geophys. Res. Atmos.* **2020**, *125* (4). https://doi.org/10.1029/2019JD030913.

(28) Gong, X.; Wex, H.; van Pinxteren, M.; Triesch, N.; Fomba, K. W.; Lubitz, J.; Stolle, C.; Robinson, T.-B.; Müller, T.; Herrmann, H.; Stratmann, F. Characterization of Aerosol Particles at Cabo Verde Close to Sea Level and at the Cloud Level – Part 2: Ice-Nucleating Particles in Air, Cloud and Seawater. *Atmos. Chem. Phys.* **2020**, *20* (3), 1451–1468.

https://doi.org/10.5194/acp-20-1451-2020.

(29) Wolf, M. J.; Goodell, M.; Dong, E.; Dove, L. A.; Zhang, C.; Franco, L. J.; Shen, C.; Rutkowski, E. G.; Narducci, D. N.; Mullen, S.; Babbin, A. R.; Cziczo, D. J. A Link between the Ice Nucleation Activity and the Biogeochemistry of Seawater. *Atmos. Chem. Phys.* **2020**, *20* (23), 15341–15356. https://doi.org/10.5194/acp-20-15341-2020.

(30) McCluskey, C. S.; Hill, T. C. J.; Malfatti, F.; Sultana, C. M.; Lee, C.; Santander, M. V; Beall, C. M.; Moore, K. A.; Cornwell, G. C.; Collins, D. B.; Prather, K. A.; Jayarathne, T.; Stone, E. A.; Azam, F.; Kreidenweis, S. M.; DeMott, P. J. A Dynamic Link between Ice Nucleating Particles Released in Nascent Sea Spray Aerosol and Oceanic Biological Activity during Two Mesocosm Experiments. *J. Atmos. Sci.* **2016**, *74* (1), 151–166. https://doi.org/10.1175/jas-d-16-0087.1.

(31) Mccluskey, C. S.; Hill, T. C. J.; Sultana, C. M.; Laskina, O.; Trueblood, J.; Santander, M. V.; Beall, C. M.; Michaud, J. M.; Kreidenweis, S. M.; Prather, K. A.; Grassian, V.; Demott, P. J. A Mesocosm Double Feature: Insights into the Chemical Makeup of Marine Ice Nucleating Particles. *J. Atmos. Sci.* **2018**, *75* (7), 2405–2423. https://doi.org/10.1175/JAS-D-17-0155.1.

(32) Riemer, N.; Ault, A. P.; West, M.; Craig, R. L.; Curtis, J. H. Aerosol Mixing State: Measurements, Modeling, and Impacts. *Rev. Geophys.* **2019**, *57* (2), 187–249. https://doi.org/10.1029/2018RG000615.

(33) Reicher, N.; Budke, C.; Eickhoff, L.; Raveh-Rubin, S.; Kaplan-Ashiri, I.; Koop, T.; Rudich, Y. Size-Dependent Ice Nucleation by Airborne Particles during Dust Events in the Eastern Mediterranean. *Atmos. Chem. Phys.* **2019**, *19* (17), 11143–11158.

https://doi.org/10.5194/acp-19-11143-2019.

(34) Mitts, B. A.; Wang, X.; Lucero, D. D.; Beall, C. M.; Deane, G. B.; DeMott, P. J.; Prather, K. A. Importance of Supermicron Ice Nucleating Particles in Nascent Sea Spray. *Geophysical Research Letters*. Blackwell Publishing Ltd February 16, 2021, p e2020GL089633. https://doi.org/10.1029/2020GL089633.

(35) Zhang, C.; Zhang, Y.; Wolf, M. J.; Nichman, L.; Shen, C.; Onasch, T. B.; Chen, L.; Cziczo, D. J. The Effects of Morphology, Mobility Size, and Secondary Organic Aerosol (SOA) Material Coating on the Ice Nucleation Activity of Black Carbon in the Cirrus Regime. *Atmos. Chem. Phys.* **2020**, *20* (22), 13957–13984. https://doi.org/10.5194/acp-20-13957-2020.

(36) Hasenkopf, C. A.; Veghte, D. P.; Schill, G. P.; Lodoysamba, S.; Freedman, M. A.; Tolbert, M. A. Ice Nucleation, Shape, and Composition of Aerosol Particles in One of the Most Polluted Cities in the World: Ulaanbaatar, Mongolia. *Atmos. Environ.* **2016**, *139*, 222–229. https://doi.org/10.1016/j.atmosenv.2016.05.037.

(37) Wagner, R.; Möhler, O. Heterogeneous Ice Nucleation Ability of Crystalline Sodium Chloride Dihydrate Particles. *J. Geophys. Res. Atmos.* **2013**, *118* (10), 4610–4622. https://doi.org/10.1002/jgrd.50325.

(38) Wagner, R.; Kaufmann, J.; Möhler, O.; Saathoff, H.; Schnaiter, M.; Ullrich, R.; Leisner, T. Heterogeneous Ice Nucleation Ability of NaCl and Sea Salt Aerosol Particles at Cirrus Temperatures. *J. Geophys. Res. Atmos.* **2018**, *123* (5), 2841–2860. https://doi.org/10.1002/2017JD027864.

(39) Wagner, R.; Ickes, L.; Bertram, A. K.; Els, N.; Gorokhova, E.; Möhler, O.; Murray, B. J.;

Umo, N. S.; Salter, M. E. Heterogeneous Ice Nucleation Ability of Aerosol Particles Generated from Arctic Sea Surface Microlayer and Surface Seawater Samples at Cirrus Temperatures. *Atmos. Chem. Phys. Discuss.* **2021**, No. April, 1–45.

(40) Peckhaus, A.; Kiselev, A.; Wagner, R.; Duft, D.; Leisner, T. Temperature-Dependent Formation of NaCl Dihydrate in Levitated NaCl and Sea Salt Aerosol Particles. *J. Chem. Phys.* **2016**, *145* (24), 244503. https://doi.org/10.1063/1.4972589.

(41) Chernoff, D. I.; Bertram, A. K. Effects of Sulfate Coatings on the Ice Nucleation Properties of a Biological Ice Nucleus and Several Types of Minerals. *J. Geophys. Res. Atmos.* **2010**, *115* (20), D20205. https://doi.org/10.1029/2010JD014254.

(42) Lee, H. D.; Wigley, S.; Lee, C.; Or, V. W.; Hasenecz, E. S.; Stone, E. A.; Grassian, V. H.; Prather, K. A.; Tivanski, A. V. Physicochemical Mixing State of Sea Spray Aerosols: Morphologies Exhibit Size Dependence. *ACS Earth Sp. Chem.* **2020**, *4* (9), 1604–1611. https://doi.org/10.1021/acsearthspacechem.0c00153.

(43) DeMott, P. J.; Hill, T. C. J.; Petters, M. D.; Bertram, A. K.; Tobo, Y.; Mason, R. H.; Suski, K. J.; Mccluskey, C. S.; Levin, E. J. T.; Schill, G. P.; Boose, Y.; Rauker, A. M.; Miller, A. J.; Zaragoza, J.; Rocci, K.; Rothfuss, N. E.; Taylor, H. P.; Hader, J. D.; Chou, C.; Huffman, J. A.; Pöschl, U.; Prenni, A. J.; Kreidenweis, S. M. Comparative Measurements of Ambient Atmospheric Concentrations of Ice Nucleating Particles Using Multiple Immersion Freezing Methods and a Continuous Flow Diffusion Chamber. *Atmos. Chem. Phys.* **2017**, *17* (18), 11227–11245. https://doi.org/10.5194/acp-17-11227-2017.

(44) Kanji, Z. A.; Abbatt, J. P. D. The University of Toronto Continuous Flow Diffusion Chamber (UT-CFDC): A Simple Design for Ice Nucleation Studies. *Aerosol Sci. Technol.*

2009, *43* (7), 730–738. https://doi.org/10.1080/02786820902889861.

(45) Hartmann, S.; Niedermeier, D.; Voigtländer, J.; Clauss, T.; Shaw, R. A.; Wex, H.; Kiselev, A.; Stratmann, F. Atmospheric Chemistry and Physics Homogeneous and Heterogeneous Ice Nucleation at LACIS: Operating Principle and Theoretical Studies. *Atmos. Chem. Phys* **2011**, *11*, 1753–1767. https://doi.org/10.5194/acp-11-1753-2011.

(46) Zobrist, B.; Marcolli, C.; Pedernera, D. A.; Koop, T. Do Atmospheric Aerosols Form Glasses? *Atmos. Chem. Phys.* **2008**, *8* (17), 5221–5244. https://doi.org/10.5194/acp-8-5221-2008.

(47) Beall, C. M.; Dale Stokes, M.; Hill, T. C.; Demott, P. J.; Dewald, J. T.; Prather, K. A. Automation and Heat Transfer Characterization of Immersion Mode Spectroscopy for Analysis of Ice Nucleating Particles. *Atmos. Meas. Tech.* **2017**, *10* (7), 2613–2626. https://doi.org/10.5194/amt-10-2613-2017.

(48) Kunert, A. T.; Lamneck, M.; Helleis, F.; Pöschl, U.; Pöhlker, M. L.; Fröhlich-Nowoisky, J. Twin-Plate Ice Nucleation Assay (TINA) with Infrared Detection for High-Throughput Droplet Freezing Experiments with Biological Ice Nuclei in Laboratory and Field Samples. *Atmos. Meas. Tech.* **2018**, *11* (11), 6327–6337. https://doi.org/10.5194/amt-11-6327-2018.

(49) Peckhaus, A.; Kiselev, A.; Hiron, T.; Ebert, M.; Leisner, T. A Comparative Study of K-Rich and Na/Ca-Rich Feldspar Ice-Nucleating Particles in a Nanoliter Droplet Freezing Assay. *Atmos. Chem. Phys.* **2016**, *16* (18), 11477–11496. https://doi.org/10.5194/acp-16-11477-2016.

(50) Taji, K.; Tachikawa, M.; Nagashima, K. Laser Trapping of Ice Crystals. *Appl. Phys. Lett.* **2006**, *88* (14), 2004–2007. https://doi.org/10.1063/1.2190074.

(51) Hoffmann, N.; Duft, D.; Kiselev, A.; Leisner, T. Contact Freezing Efficiency of Mineral Dust Aerosols Studied in an Electrodynamic Balance: Quantitative Size and Temperature Dependence for Illite Particles. *Faraday Discuss.* **2013**, *165* (0), 383–390. https://doi.org/10.1039/c3fd00033h.

(52) You, Y.; Renbaum-Wolff, L.; Carreras-Sospedra, M.; Hanna, S. J.; Hiranuma, N.; Kamal, S.; Smith, M. L.; Zhang, X.; Weber, R. J.; Shilling, J. E.; Dabdub, D.; Martin, S. T.; Bertram, A. K. Images Reveal That Atmospheric Particles Can Undergo Liquid-Liquid Phase Separations. *Proc. Natl. Acad. Sci.* **2012**, *109* (33), 13188–13193. https://doi.org/10.1073/pnas.1206414109.

(53) McMurry, P. H.; Litchy, M.; Huang, P. F.; Cai, X.; Turpin, B. J.; Dick, W. D.; Hanson, A. Elemental Composition and Morphology of Individual Particles Separated by Size and Hygroscopicity with the TDMA. *Atmos. Environ.* **1996**, *30* (1), 101–108. https://doi.org/10.1016/1352-2310(95)00235-Q.

(54) Zardini, A. A.; Sjogren, S.; Marcolli, C.; Krieger, U. K.; Gysel, M.; Weingartner, E.; Baltensperger, U.; Peter, T. A Combined Particle Trap/HTDMA Hygroscopicity Study of Mixed Inorganic/Organic Aerosol Particles. *Atmos. Chem. Phys.* **2008**, *8* (18), 5589–5601. https://doi.org/10.5194/acp-8-5589-2008.

(55) Bateman, A. P.; Belassein, H.; Martin, S. T. Impactor Apparatus for the Study of Particle Rebound: Relative Humidity and Capillary Forces. *Aerosol Sci. Technol.* **2014**, *48* (1), 42–52. https://doi.org/10.1080/02786826.2013.853866.

(56) Tarn, M. D.; Sikora, S. N. F.; Porter, G. C. E.; O'Sullivan, D.; Adams, M.; Whale, T. F.; Harrison, A. D.; Vergara-Temprado, J.; Wilson, T. W.; Shim, J. uk; Murray, B. J. The Study

of Atmospheric Ice-Nucleating Particles via Microfluidically Generated Droplets. *Microfluid. Nanofluidics* **2018**, *22* (5), 1–25. https://doi.org/10.1007/s10404-018-2069-x.

(57) Brubaker, T.; Polen, M.; Cheng, P.; Ekambaram, V.; Somers, J.; Anna, S. L.; Sullivan, R. C. Development and Characterization of a "Store and Create" Microfluidic Device to Determine the Heterogeneous Freezing Properties of Ice Nucleating Particles. *Aerosol Sci. Technol.* **2020**, *54* (1), 79–93. https://doi.org/10.1080/02786826.2019.1679349.

(58) Reicher, N.; Segev, L.; Rudich, Y. The WeIzmann Supercooled Droplets Observation on a Microarray (WISDOM) and Application for Ambient Dust. *Atmos. Meas. Tech.* **2018**, *11* (1), 233–248. https://doi.org/10.5194/amt-11-233-2018.

(59) Tarn, M. D.; Sikora, S. N. F.; Porter, G. C. E.; Wyld, B. V.; Alayof, M.; Reicher, N.; Harrison, A. D.; Rudich, Y.; Shim, J. U.; Murray, B. J. On-Chip Analysis of Atmospheric Ice-Nucleating Particles in Continuous Flow. *Lab Chip* **2020**, *20* (16), 2889–2910. https://doi.org/10.1039/d0lc00251h.

(60) Stan, C. A.; Schneider, G. F.; Shevkoplyas, S. S.; Hashimoto, M.; Ibanescu, M.; Wiley, B. J.; Whitesides, G. M. A Microfluidic Apparatus for the Study of Ice Nucleation in Supercooled Water Drops. *Lab Chip* **2009**, *9* (16), 2293. https://doi.org/10.1039/b906198c.

(61) Roy, P.; House, M. L.; Dutcher, C. S. A Microfluidic Device for Automated High Throughput Detection of Ice Nucleation of Snomax®. *Micromachines* **2021**, *12* (3), 296. https://doi.org/10.3390/mi12030296.

(62) Nandy, L.; Dutcher, C. S. Phase Behavior of Ammonium Sulfate with Organic Acid Solutions in Aqueous Aerosol Mimics Using Microfluidic Traps. *J. Phys. Chem. B* **2018**, *122* (13), 3480–3490. https://doi.org/10.1021/acs.jpcb.7b10655.

(63) Nandy, L.; Liu, S.; Gunsbury, C.; Wang, X.; Pendergraft, M. A.; Prather, K. A.; Dutcher, C. S. Multistep Phase Transitions in Sea Surface Microlayer Droplets and Aerosol Mimics Using Microfluidic Wells. *ACS Earth Sp. Chem.* **2019**, *3* (7), 1260–1267. https://doi.org/10.1021/acsearthspacechem.9b00121.

(64) Roy, P.; Mael, L. E.; Makhnenko, I.; Martz, R.; Grassian, V. H.; Dutcher, C. S. Temperature-Dependent Phase Transitions of Aqueous Aerosol Droplet Systems in Microfluidic Traps. *ACS Earth Sp. Chem.* **2020**, *4* (9), 1527–1539. https://doi.org/10.1021/acsearthspacechem.0c00114.

(65) Roy, P.; Liu, S.; Dutcher, C. S. Droplet Interfacial Tensions and Phase Transitions Measured in Microfluidic Channels. *Annu. Rev. Phys. Chem.* **2021**, *72* (1), 73–97. https://doi.org/10.1146/annurev-physchem-090419-105522.

(66) Sauer, J. S.; Mayer, K. J.; Lee, C.; Alves, M. R.; Amiri, S.; Bahaveolos, C.; Barnes, E. B.; Crocker, D. R.; Dinasquet, J.; Garofalo, L. A.; Kaluarachchi, C. P.; Dang, D.; Kilgour, D.; Mael, L.; Mitts, B. A.; Moon, D. R.; Morris, C. K.; Moore, A. N.; Ni, C.-M.; Pendergraft, M. A.; Petras, D.; Simpson, R.; Smith, S.; Tumminello, P. R.; Walker, J. L.; DeMott, P. J.; Farmer, D. K.; Goldstein, A. H.; Grassian, V. H.; Jaffe, J. S.; Malfatti, F.; Martz, T. R.; Slade, J.; Tivanski, A. V.; Bertram, T. H.; Cappa, C. D.; Prather, K. A. The Sea Spray Chemistry and Particle Evolution Study (SeaSCAPE): Overview and Experimental Methods. *Environ. Sci. Process. Impacts*.

(67) Cunliffe, M.; Wurl, O. Sampling the Sea Surface Microlayer; Springer, Berlin, Heidelberg, 2015; pp 255–261. https://doi.org/10.1007/8623_2015_83.

(68) Sun, M.; Bithi, S. S.; Vanapalli, S. A. Microfluidic Static Droplet Arrays with Tuneable

Gradients in Material Composition. *Lab Chip* **2011**, *11* (23), 3949–3952. https://doi.org/10.1039/c1lc20709a.

(69) Vali, G. Quantitative Evaluation of Experimental Results an the Heterogeneous Freezing Nucleation of Supercooled Liquids. *J. Atmos. Sci.* **1971**, *28* (3), 402–409. https://doi.org/10.1175/1520-0469(1971)028<0402:QEOERA>2.0.CO;2.

(70) Agresti, A.; Coull, B. A. Approximate Is Better than "Exact" for Interval Estimation of Binomial Proportions. *Am. Stat.* **1998**, *52* (2), 119–126. https://doi.org/10.1080/00031305.1998.10480550.

(71) Mael, L. E.; Busse, H.; Grassian, V. H. Measurements of Immersion Freezing and Heterogeneous Chemistry of Atmospherically Relevant Single Particles with Micro-Raman Spectroscopy. *Anal. Chem.* **2019**, *91* (17), 11138–11145. https://doi.org/10.1021/acs.analchem.9b01819.

(72) Barry, K. R.; Hill, T. C. J.; Jentzsch, C.; Moffett, B. F.; Stratmann, F.; DeMott, P. J. Pragmatic Protocols for Working Cleanly When Measuring Ice Nucleating Particles. *Atmos. Res.* **2021**, *250*, 105419. https://doi.org/10.1016/j.atmosres.2020.105419.

(73) Hiranuma, N.; Augustin-Bauditz, S.; Bingemer, H.; Budke, C.; Curtius, J.; Danielczok, A.; Diehl, K.; Dreischmeier, K.; Ebert, M.; Frank, F.; Hoffmann, N.; Kandler, K.; Kiselev, A.; Koop, T.; Leisner, T.; Möhler, O.; Nillius, B.; Peckhaus, A.; Rose, D.; Weinbruch, S.; Wex, H.; Boose, Y.; Demott, P. J.; Hader, J. D.; Hill, T. C. J.; Kanji, Z. A.; Kulkarni, G.; Levin, E. J. T.; McCluskey, C. S.; Murakami, M.; Murray, B. J.; Niedermeier, D.; Petters, M. D.; O'Sullivan, D.; Saito, A.; Schill, G. P.; Tajiri, T.; Tolbert, M. A.; Welti, A.; Whale, T. F.; Wright, T. P.; Yamashita, K. A Comprehensive Laboratory Study on the Immersion

Freezing Behavior of Illite NX Particles: A Comparison of 17 Ice Nucleation Measurement Techniques. *Atmos. Chem. Phys.* **2015**, *15* (5), 2489–2518. https://doi.org/10.5194/acp-15-2489-2015.

(74) Suski, K. J.; Hill, T. C. J.; Levin, E. J. T.; Miller, A.; DeMott, P. J.; Kreidenweis, S. M. Agricultural Harvesting Emissions of Ice-Nucleating Particles. *Atmos. Chem. Phys.* **2018**, *18* (18), 13755–13771. https://doi.org/10.5194/acp-18-13755-2018.

(75) Polen, M.; Brubaker, T.; Somers, J.; Sullivan, R. C. Cleaning up Our Water: Reducing Interferences from Nonhomogeneous Freezing of "Pure" Water in Droplet Freezing Assays of Ice-Nucleating Particles. *Atmos. Meas. Tech.* **2018**, *11* (9), 5315–5334. https://doi.org/10.5194/amt-11-5315-2018.

(76) Wang, A.; Freeman, J. J.; Jolliff, B. L.; Chou, I. M. Sulfates on Mars: A Systematic Raman Spectroscopic Study of Hydration States of Magnesium Sulfates. *Geochim. Cosmochim. Acta* **2006**, *70* (24), 6118–6135. https://doi.org/10.1016/j.gca.2006.05.022.

(77) Ault, A. P.; Zhao, D.; Ebben, C. J.; Tauber, M. J.; Geiger, F. M.; Prather, K. A.; Grassian, V. H. Raman Microspectroscopy and Vibrational Sum Frequency Generation Spectroscopy as Probes of the Bulk and Surface Compositions of Size-Resolved Sea Spray Aerosol Particles. *Phys. Chem. Chem. Phys.* **2013**, *15* (17), 6206–6214. https://doi.org/10.1039/c3cp43899f.

(78) Schulz, H.; Baranska, M.; Baranski, R. Potential of NIR-FT-Raman Spectroscopy in Natural Carotenoid Analysis. *Biopolymers* **2005**, *77* (4), 212–221. https://doi.org/10.1002/bip.20215.

(79) Cochran, R. E.; Laskina, O.; Trueblood, J. V.; Estillore, A. D.; Morris, H. S.; Jayarathne,

T.; Sultana, C. M.; Lee, C.; Lin, P.; Laskin, J.; Laskin, A.; Dowling, J. A.; Qin, Z.; Cappa, C. D.; Bertram, T. H.; Tivanski, A. V.; Stone, E. A.; Prather, K. A.; Grassian, V. H. Molecular Diversity of Sea Spray Aerosol Particles: Impact of Ocean Biology on Particle Composition and Hygroscopicity. *Chem* **2017**, *2* (5), 655–667. https://doi.org/10.1016/j.chempr.2017.03.007.

(80) Ickes, L.; Porter, G. C. E.; Wagner, R.; Adams, M. P.; Bierbauer, S.; Bertram, A. K.; Bilde, M.; Christiansen, S.; Ekman, A. M. L.; Gorokhova, E.; Höhler, K.; Kiselev, A. A.; Leck, C.; Möhler, O.; Murray, B. J.; Schiebel, T.; Ullrich, R.; Salter, M. E. The Ice-Nucleating Activity of Arctic Sea Surface Microlayer Samples and Marine Algal Cultures. *Atmos. Chem. Phys.* **2020**, *20* (18), 11089–11117. https://doi.org/10.5194/acp-20-11089-2020.

(81) Wang, X.; Sultana, C. M.; Trueblood, J.; Hill, T. C. J.; Malfatti, F.; Lee, C.; Laskina, O.; Moore, K. A.; Beall, C. M.; McCluskey, C. S.; Cornwell, G. C.; Zhou, Y.; Cox, J. L.; Pendergraft, M. A.; Santander, M. V.; Bertram, T. H.; Cappa, C. D.; Azam, F.; DeMott, P. J.; Grassian, V. H.; Prather, K. A. Microbial Control of Sea Spray Aerosol Composition: A Tale of Two Blooms. *ACS Cent. Sci.* **2015**, *1* (3), 124–131. https://doi.org/10.1021/acscentsci.5b00148.

(82) Knopf, D. A.; Alpert, P. A.; Wang, B.; Aller, J. Y. Stimulation of Ice Nucleation by Marine Diatoms. **2010**. https://doi.org/10.1038/NGEO1037.

(83) Wagstaff, B. A.; Rejzek, M.; Field, R. A. Identification of a Kdn Biosynthesis Pathway in the Haptophyte Prymnesium Parvum Suggests Widespread Sialic Acid Biosynthesis among Microalgae. *J. Biol. Chem.* **2018**, *293* (42), 16277–16290. https://doi.org/10.1074/jbc.RA118.004921.

TOC Graphic